Thermal conductivity of diamond under extreme pressure: A first-principles study

D. A. Broido, L. Lindsay, and A. Ward

Phys. Rev. B **86**, 115203 — Published 6 September 2012

DOI: 10.1103/PhysRevB.86.115203

Thermal conductivity of diamond under extreme pressure: A first principles study

D. A. Broido[1], L. Lindsay[2], and A. Ward[3]

[1]Department of Physics, Boston College, Chestnut Hill, Massachusetts 02467, USA

[2]Naval Research Laboratory, Washington, D.C. 20375, USA

[3]Department of Biology, Boston College, Chestnut Hill, Massachusetts 02467, USA

Abstract

Using a first principles approach based on density functional perturbation theory and an exact numerical solution to the phonon Boltzmann equation, we show that application of large compressive hydrostatic pressure dramatically increases the thermal conductivity of diamond. We connect this enhancement to the overall increased frequency scale with pressure, which makes acoustic velocities larger and reduces phonon-phonon scattering rates. Of particular importance is the often neglected fact that heat-carrying acoustic phonons are coupled through lattice anharmonicity to higher frequency optic modes. An increase in optic mode frequencies with pressure weakens this coupling and contributes to driving the diamond thermal conductivities to far larger values than in any material at ambient pressure and temperature.

PACS: 66.70.-f, 63.20.kg, 71.15Mb

I. Introduction

Diamond has a number of remarkable properties including unparalleled mechanical strength and transparency, and unusually high incompressibility, melting temperature, and thermal conductivity [1]. It is a covalent insulator with simple electronic and lattice structures. As a result, diamond has for decades been the subject of intense investigation, both for scientific understanding as well as for technological applications.

Recently, considerable attention has been focused on the properties of diamond under extreme pressure in connection to planetary astrophysics [2, 3], to capsules for inertially confined fusion [4], and to the understanding of processes deep within the Earth [5]. Diamond has also proven to be an ideal test material for both theoretical [6-8] and experimental [9-11] high-pressure studies with measured pressures reaching as high as 800GPa [11].

In this work we examine theoretically the thermal conductivity, k, of diamond under large compressive hydrostatic pressure. The pressure dependence of the thermal conductivity of non-metals was first studied almost a century ago by Bridgeman [12]. He found increases in k with pressure, P. Many subsequent measurements over the intervening decades corroborated this behavior in a variety of materials including Alkali Halides [13-15], ice [16, 17], and those relevant to heat flow in the earth's mantle such as MgO [18]. Considerable progress has also been achieved in developing accurate measurement techniques of $k(P)$ [15, 18-21], with P extending up to several tens of GPa.

The intrinsic thermal conductivity of insulators is governed by phonon-phonon interactions arising from the anharmonicity of the interatomic potential [22]. As a result of the complexity of accurately representing this interaction theoretical descriptions of $k(P)$ have frequently relied on the simple Leibfried and Schlömann model [23, 24], which makes many approximations and also

assumes that the temperature range considered is well above the Debye temperature, θ_D. Over the past few years, quantitative first principles approaches have been developed to calculate the thermal conductivity of semiconductors and insulators [25-38], and some of these were directly applied to examine the *k(P)* for MgO [27, 30, 31].

The pressure dependence of the thermal conductivity of diamond should be particularly interesting. At ambient pressure and temperature, diamond has the highest thermal conductivity, k_0, of any bulk 3D material with recorded values for isotopically enriched crystals around 3000W/m^{-1}K^{-1} [39], over seven times higher than copper. This high value arises from stiff atomic bonds and light carbon mass. Diamond's unusually small compressibility allows it to withstand pressures exceeding 1000 GPa without undergoing a structural phase transition. Thus, one might expect that record thermal conductivity values could be achieved in diamond under high pressure conditions.

In this work we demonstrate this behavior using a first principles approach, which combines accurate calculation of the harmonic and anharmonic interatomic force constants (IFCs) using density functional perturbation theory (DFPT) with an exact numerical solution to the Peierls-Boltzmann transport equation (PBE) for phonons [25, 26, 40, 41]. Previous implementation of this approach for ambient pressure yielded excellent agreement with the measured thermal conductivities of silicon, germanium and diamond [25, 26] with no adjustable parameters. At pressures of several hundred GPa, we find calculated *k(P)* values that are several times higher than k_0 and thus far higher thermal conductivities than occur in any known material at ambient pressure and temperature. The origin of this behavior is connected to the change in intrinsic anharmonic interaction between phonons. A shift of the phonons to high frequencies with pressure weakens this interaction, which leads to large increases in thermal conductivity. In

particular, the often-neglected coupling of the heat-carrying acoustic phonons to the optic modes plays a crucial role. While optic phonons are frequently neglected in thermal conductivity calculations [23, 24] because they carry little heat, these phonons provide essential scattering channels for the acoustic phonons. Their shift to higher frequency with pressure is a key factor in driving up the thermal conductivity. These findings are consistent with previous *ab initio* calculations [25, 26, 36, 37, 42] which have noted that acoustic-optic mode coupling should play an important role in determining the thermal conductivity of a material. In addition, recent measurements and theory have found it to explain the anomalously low thermal conductivity observed in PbTe [36, 37].

In Section II, a description of the theoretical approach used here to calculate the thermal conductivity of diamond under pressure is given. Section III presents and discusses our results. To connect to previous theories, we will also discuss in this section the application to diamond of the Leibfried and Schlömann model [23] as well as previous first principles approaches [27, 30, 31]. We will show that these theories are not appropriate for diamond because of its stiff lattice and resulting high phonon frequency scale. Section IV presents a summary of our findings.

II. *Ab initio* Transport Theory.

In diamond, heat is predominantly carried by phonons. A temperature gradient, ∇T, drives a phonon heat current $\mathbf{J}_Q = (1/V)\sum_\lambda \hbar\omega_\lambda \mathbf{v}_\lambda n_\lambda$ through the sample. The sum is over all phonon modes $\lambda = (\mathbf{q}, j)$ with $\mathbf{q}$ being the phonon wave vector and j labeling the phonon polarization, ω_λ and $\mathbf{v}_\lambda$ are the phonon frequency and velocity in mode λ and V is the crystal volume. For small ∇T, the non-equilibrium distribution function, $n_\lambda = n_\lambda^0 + n_\lambda^1$, can be determined by solving the linearized PBE. Here, $n_\lambda^0 = 1/(\exp(\hbar\omega_\lambda / k_B T) - 1)$ is the Bose factor at temperature T,

and $n_\lambda^1 = -(dn_\lambda^0/dT)\sum_\alpha v_{\lambda\alpha}\tau_{\lambda\alpha}dT/dx_\alpha$, where the sum is over the Cartesian components, x, y and z taken to be along the cubic axes. Note that n_λ^1 is explicitly related to $\tau_{\lambda\alpha}$, the phonon lifetime in mode λ for temperature gradient along direction α [22, 43].

Phonons are scattered by other phonons through intrinsic anharmonic processes, or by extrinsic processes such as isotopic impurities, defects, and crystal boundaries [22]. The phonon lifetime $\tau_{\lambda\alpha}$ due to this scattering can be extracted from the solution of the linearized PBE [25, 26, 41, 42], which can be cast as a set of coupled equations for $\tau_{\lambda\alpha}$:

$$\tau_{\lambda\alpha} = \tau_\lambda^0 + \tau_\lambda^0\left[\sum_+ \Delta^{(+)}(\Gamma^{(+)}_{\lambda\lambda'\lambda''}, \tau_{\lambda'\alpha}\tau_{\lambda''\alpha}) + \sum_- \Delta^{(-)}(\Gamma^{(-)}_{\lambda\lambda'\lambda''}, \tau_{\lambda'\alpha}\tau_{\lambda''\alpha})\right] \qquad (1)$$

In Eq. 1 the sums are over all of the modes λ′, and λ″ satisfying energy and momentum conservation conditions for "+" and "-" three-phonon scattering processes:

$$\omega_\lambda \pm \omega_{\lambda'} = \omega_{\lambda''} \text{ and } \mathbf{q} \pm \mathbf{q}' = \mathbf{q}'' + \mathbf{K} \qquad (2)$$

where **K** is a reciprocal lattice vector, which is zero for momentum-conserving Normal processes and non-zero for resistive Umklapp processes. The functions $\Delta^{(\pm)}$ depend on phonon lifetimes in modes λ′, and λ″ and on $\Gamma^{(+)}_{\lambda\lambda'\lambda''}$ and $\Gamma^{(-)}_{\lambda\lambda'\lambda''}$, the intrinsic anharmonic scattering rates for processes satisfying Eq. 2. These scattering rates are obtained to lowest-order in perturbation theory and describe the interaction of three phonons. τ_λ^0 is given by:

$$1/\tau_\lambda^0 \equiv \sum_{\lambda'\lambda''}^{(+)} \Gamma^{(+)}_{\lambda\lambda'\lambda''} + 1/2\sum_{\lambda'\lambda''}^{(-)} \Gamma^{(-)}_{\lambda\lambda'\lambda''} + 1/\tau_\lambda^{ext} \qquad (3)$$

where the intrinsic three-phonon scattering probabilities are:

$$\Gamma^{(\pm)}_{\lambda\lambda'\lambda''} = \frac{\hbar\pi}{4N_0\omega_\lambda\omega_{\lambda'}\omega_{\lambda''}}\begin{Bmatrix} n^0_{\lambda'} - n^0_{\lambda''} \\ n^0_{\lambda'} + n^0_{\lambda''} + 1 \end{Bmatrix}\left|\Phi^{(\pm)}_{\lambda,\pm\lambda',-\lambda''}\right|^2 \delta(\omega_\lambda \pm \omega_{\lambda'} - \omega_{\lambda''}) \qquad (4)$$

In Eq. 4, N_0 is the number of unit cells, and the three-phonon matrix elements are given by

$$\Phi_{\lambda\lambda'\lambda''} = \sum_{\kappa}\sum_{l'\kappa'}\sum_{l''\kappa''}\sum_{\alpha\beta\gamma}\Phi_{\alpha\beta\gamma}(0\kappa, l'\kappa', l''\kappa'')\frac{e^{\lambda}_{\alpha\kappa}e^{\lambda'}_{\beta\kappa'}e^{\lambda''}_{\gamma\kappa''}}{\sqrt{M_{\kappa}M_{\kappa'}M_{\kappa''}}}e^{i\mathbf{q}'\cdot\mathbf{R}_{l'}}e^{i\mathbf{q}''\cdot\mathbf{R}_{l''}} \quad (5)$$

where $\Phi_{\alpha\beta\gamma}(0\kappa, l'\kappa', l''\kappa'')$ are the third-order anharmonic IFCs, $e^{\lambda}_{\alpha\kappa}$ is the α^{th} component of the phonon eigenvector for the κ^{th} atom in the unit cell with mass M_{κ} and in mode λ, and $\mathbf{R}_l$ is the lattice vector locating the l^{th} unit cell. In Eq. 3 $1/\tau^{ext}_{\lambda}$ are the scattering rates due to extrinsic processes, to be specified below.

The lattice thermal conductivity, k_L, is a scalar for cubic crystals such as diamond [22]:

$$k_L \equiv k_{\alpha\alpha} = \sum_{\lambda} C_{\lambda} v^2_{\lambda\alpha}\tau_{\lambda\alpha} \quad (6)$$

where $C_{\lambda} = k_B n^0_{\lambda}(n^0_{\lambda}+1)(\hbar\omega_{\lambda}/k_B T)^2/V$ is the specific heat capacity per phonon mode. The solution to the PBE, Eq. 1, has been described in detail elsewhere [25, 26, 40, 41]. Here we focus on the physical significance of its components. τ^0_{λ} is directly determined from the combined scattering rates for all intrinsic and extrinsic processes. Of particular importance, Normal processes are treated as resistive. In principle, this is incorrect since Normal processes do not change the heat current [22, 25, 26, 40, 41, 43]. The thermal conductivity, k^0_L, obtained using τ^0_{λ} in place of τ_{λ} in Eq. 6 therefore underestimates k_L. The full PBE solution for $\tau_{\lambda\alpha}$ corrects for this giving $k_L = k^0_L + \Delta k$ where $\Delta k > 0$. For temperatures $T \sim \theta_D$, Umklapp scattering dominates Normal scattering so Δk is typically small. Diamond has θ_D~2000K so around and below room temperature, $T << \theta_D$ and Δk is large and must be explicitly included in the full PBE solution to accurately describe k_L [26].

The total energy, $E(V)$, hydrostatic pressure, $P = -\partial E/\partial V$ and harmonic IFCs were calculated *ab initio* using the Quantum Espresso package [44], while anharmonic IFCs were generated

following the approach of Ref. 45. All IFCs for each *P* were determined within the framework of DFPT and the local density approximation (LDA), using the BHS pseudopotential [46]. The harmonic IFCs were calculated using a 6x6x6 Monkhorst-Pack [47] k-point mesh while the anharmonic IFCs were determined using a 4x4x4 mesh and including interactions out to seventh nearest neighbors [25, 26, 45]. Phonon frequencies and eigenvectors are obtained from the harmonic IFCs while phonon-phonon scattering rates require both harmonic and anharmonic IFCs. We highlight that our approach introduces *no adjustable parameters*.

III. Results and Discussion

We calculate k_L for diamond as a function of *T* and *P*. We ignore defects other than isotopes so our calculations best compare with type IIa diamond [40], the purest type. Both naturally occurring isotope concentration (1.1% ^{13}C) [39] and a hypothetical isotopically pure (i.e. 100% ^{12}C) material are investigated. The phonon-isotope scattering rate can be written in the polarization-independent closed form [48]: $1/\tau_\lambda^{iso} \equiv 1/\tau^{iso}(\omega) = \pi V_0 g \omega^2 D(\omega)/6$, where $D(\omega)$ is the phonon density of states, $V_0 = a^3/8$ is the volume per atom where *a* is the zero-temperature lattice constant, *g* is the mass variance parameter ($g = 7.54 \times 10^{-5}$ for diamond with 1.1% C^{13} impurities in C^{12} [26]). The effect of phonon scattering from sample boundaries has been included through an empirical scattering time: $\tau_b = L/|\mathbf{v}_\lambda|$ where *L* is the effective sample size [22].

Figure 1 shows our calculated pressure as a function of the lattice constant (solid red curve), reflecting the equation of state for diamond, and it demonstrates excellent agreement with LDA results obtained previously in Ref. 6 (open circles). Also represented by the solid black squares are the measured results from Ref. 9, which extend up to 140 GPa. These data are in good agreement with the calculated values. They lie slightly higher than the calculated results because

the LDA has a tendency to overbind giving total-energy-minimized lattice constants that are about 1% smaller than that measured for diamond. Figure 2 shows the phonon density of states for diamond at ambient pressure, P=0 and at P=125 GPa. Compressive pressure barely changes the low frequency transverse acoustic (TA) phonons but shifts the longitudinal acoustic (LA) phonons and the optic phonons to larger frequencies, as has been demonstrated previously [6-9].

Figure 3 shows k_L as a function of T for P=0 (solid and dashed black curves) and P=125GPa (solid and dashed red curves). Two cases are considered: k_{nat} is the thermal conductivity for naturally occurring diamond with 1.1% ^{13}C isotopic impurities. k_{pure} is for the hypothetical case of no isotopic impurities. We have taken a sample size L=1mm consistent with previously chosen values for diamond [49]. For low temperature, the boundary scattering term dominates with $k_L \sim T^3$ for all cases. In this regime, the slightly increased acoustic phonon velocities at high P enhance the boundary scattering causing the observed slightly smaller k_L values. Above the peaks, phonon-phonon scattering provides the dominant thermal resistance. In this regime lowering T decreases the thermal occupation of phonons at all frequencies causing the phonon-phonon scattering rates to decrease and k_{nat} and k_{pure} to rise. We note that for P=0, our previously calculated k_L as a function of temperature [26] was found to be in very good agreement with measured values [39, 49-51]. For P=125GPa k_{nat} and k_{pure} remain several times larger than the corresponding $P=0$ values throughout the range of temperatures above the peaks. As a result, the peak locations shift to higher T. In the vicinity of the peaks, the isotope effect for both cases becomes enormous with enhancement factors k_{pure}/ k_{nat} of roughly seven.

Figure 4 shows k_{nat} and k_{pure} as a function of P at T=300K calculated using the *ab initio* approach described above. For $P=0$ k_{nat}=2290 $Wm^{-1}K^{-1}$, while k_{pure} =3450 $Wm^{-1}K^{-1}$, about 50% larger than k_{nat} due to removal of the phonon isotope scattering. With increasing P k_{nat}

and k_{pure} become much larger; at 400GPa, k_{nat}≈12000 $Wm^{-1}K^{-1}$ and k_{pure} =17000$Wm^{-1}K^{-1}$ corresponding to nearly five-fold increases compared to the *P=0* values. These values are far higher than those in any known material at ambient *P* and *T*.

The dramatic increase in k_L with pressure is connected to the intrinsic anharmonic coupling between phonons. Our calculational scheme allows us to examine this coupling through the behavior of the momentum and energy conserving three-phonon processes. The types of processes that dominate the three-phonon scattering rates for acoustic phonons are: $a + a \leftrightarrow a$ and $a + a \rightarrow o$. Here *a* and *o* refer to acoustic and optic phonons, respectively. The processes involving only acoustic phonons i.e. the $a + a \leftrightarrow a$ contributions to the scattering rates dominate at lower frequencies while at higher frequencies a cross-over takes place in which the processes involving optic modes i.e. $a + a \rightarrow o$ become the most important. In comparing $a + a \leftrightarrow a$ and $a + a \rightarrow o$ processes, we find that vast majority of Umklapp processes are of the $a + a \rightarrow o$ type. This makes sense since the $a + a \rightarrow o$ processes typically involve larger wave vector acoustic phonons. However, it is important to note that both $a + a \leftrightarrow a$ and $a + a \rightarrow o$ processes are required to accurately describe k_L. Removal of either type gives far too high k_L.values.

In many theoretical treatments of thermal conductivity, only acoustic phonons are included. However, the importance of the coupling between acoustic and optic modes in diamond has been noted previously [26, 52, 53]. While optic phonons carry little heat they are key participants in phonon-phonon scattering processes that limit k_L. In diamond at *P*=0, about 80% of the three-phonon processes contributing to the total acoustic branch scattering rates involve optic phonons [26, 52]. Thus, removal of the acoustic-optic mode scattering channels causes k_L to rise significantly with over a six-fold increase at room temperature [26].

With increasing P, both acoustic and optic phonon modes involved in three-phonon scattering processes shift to higher frequencies. As a result, the acoustic phonon velocities become larger, but this is relatively modest, around 5% for the TA branch and around 15% for the LA branch for P=125GPa. The increase in k_L produced by this velocity change represents only a small fraction of that observed in Figs. 3 and 4. The overall higher phonon frequencies with pressure are responsible for the majority of the increase in k_L since this dramatically decreases the three-phonon scattering rates.. To highlight the connection between the optic phonon frequencies and k_L the inset to Fig. 4 shows the calculated maximum optic phonon frequency, ω_{LTO}, plotted against P [53]. It is evident that the rise in ω_{LTO} with P tracks with the corresponding increase in k_L.

One can ask about the effect of pressure on the anharmonic IFCs since any changes in the anharmonic IFCs must also affect k_L in conjunction with those from the harmonic IFCs. We find that anharmonic IFCs increase in magnitude with increasing P, just as do the harmonic IFCs. Since the anharmonic IFCs enter the three-phonon scattering matrix elements, Eq. 5, this means that the harmonic and anharmonic IFCs work in opposition, the former acting to increase k_L while the latter acting to decrease it. To appreciate this point, we have mixed harmonic and anharmonic IFCs at two different pressures, P=0 and P=125GPa. For case 1, we combine the harmonic IFCs at P=0 and the anharmonic IFCs at P=125GPa. For case 2, we reverse these, with harmonic IFCs at P=125GPa combined with the anharmonic IFCs at P=0. At T=300K, we obtain k_{pure} =1170Wm^{-1}K^{-1} for case 1 and k_{pure} =18,690Wm^{-1}K^{-1} for case 2. These numbers are to be compared to the actual values of k_{pure}=3450Wm^{-1}K^{-1} for P=0 and k_{pure}=6880Wm^{-1}K^{-1} for P=125GPa. Thus, the increase of the harmonic IFCs with pressure is a more important driver of k_L than that for the anharmonic IFCs. Nevertheless, the increasing

anharmonic IFCs with pressure play an important role in suppressing what would be an even larger increase in k_L.

In the T regime where phonon-phonon scattering dominates, both decreasing T and increasing P cause k_L to increase. However, the effects of these changes on the spectral distribution of phonons contributing to k_L are decidedly different. To illustrate this we calculate the accumulated thermal conductivity $k_{acc}(l)$, which adds up all contributions to k_L from phonons with scattering lengths $|\mathbf{v}_\lambda|\tau_{\lambda z}$ less than l:

$$k_{acc}(l) = \sum_{\lambda} C_\lambda v_{\lambda z}^2 \tau_{\lambda z} \theta(l - |\mathbf{v}_\lambda|\tau_{\lambda z}) \tag{7}$$

For clarity, we consider the isotopically pure case where only phonon-phonon scattering is included. Figure 5 shows the ratio $k_{acc}(l)/k_L$ for three cases. The solid black curve gives $k_{acc}(l)/k_L$ for P=0 and T=300K. For this case, about 80% of the contributions to k_L come for l between 0.5μm and 2μm. The spectral distribution is relatively narrow since $T<<\theta_D$ so only a small portion of the heat carrying acoustic phonon spectrum is thermally populated. The blue curve shows $k_{acc}(l)/k_L$ for P=0 and T=200K. This curve is similar to the previous case but shifted to larger scattering lengths, highlighting that lowering the temperature increases the scattering lengths of all phonon modes contributing to k_L. The dotted red curve gives the $k_{acc}(l)/k_L$ for P=125GPa and T=300K. It shows that increasing pressure predominantly affects phonons with larger intrinsic scattering lengths. This can be understood as follows. Increasing P shifts primarily the LA and optic phonon modes to higher frequency thereby decreasing their populations. As a result, the scattering rates for low frequency acoustic phonons are substantially reduced since these phonons are mainly coupled through the anharmonic interaction to optic phonons. This gives increased $|\mathbf{v}_\lambda|\tau_{\lambda z}$. However, we find that with increasing P the

number of three-phonon scattering processes satisfying Eq. 2 actually becomes larger for higher frequency acoustic phonons. This counteracts somewhat the effect of the suppressed *LA* and optic phonon populations and gives three-phonon scattering rates and $|\mathbf{v}_\lambda|\tau_{\lambda z}$ closer to those at *P*=0. This results in the more extended spectral distribution illustrated in Fig. 5.

The above description for increasing k_L with *P* can be directly connected to the relative strengths of Normal and Umklapp scattering processes. Normal processes typically involve lower frequency phonons than Umklapp processes. From the above discussion, we expect that with increasing *P* the scattering rates due to Normal processes will be weakened relative to their Umklapp counterparts. As a result the correction factor, Δk, coming from proper treatment of Normal processes (see text below Eq. 6) should become a smaller fraction of k_L. This is exactly what we find. At room temperature, $\Delta k/k_L = 0.31$ for *P*=0 while *P*=125GPa, $\Delta k/k_L = 0.16$.

We now examine previously developed theories to calculate $k_L(P)$. The most commonly used theory to describe the pressure dependence of thermal conductivity is that given by Leibfried and Schlömann [23], which gives $k_L = AV_0^{1/3}\omega_D^3/\bar{\gamma}^2 T$ where *A* is a pressure independent constant, ω_D is the Debye frequency and $\bar{\gamma}$ is an averaged Grüneisen parameter, taken as a measure of the strength of the anharmonic scattering. Within the Debye model, $\omega_D = \bar{v}q_D$ with $\bar{v}$ being the averaged acoustic velocity defined by $\bar{v} = 3/(2/v_{TA} + 1/v_{LA})$ where v_{TA} (v_{LA}) is the transverse (longitudinal) acoustic phonon velocity, and the Debye wavevector $q_D \sim V_0^{-1/3}$. For $\bar{\gamma}$ we employ the commonly used mode-averaged expression: $\bar{\gamma} = \sum_\lambda C_\lambda \gamma_\lambda / \sum_\lambda C_\lambda$ where $\gamma_\lambda = -d\ln\omega_\lambda / d\ln V$ is the Grüneisen parameter for mode λ and C_λ was defined below Eq. 6. The mode Grüneisen parameters can be expressed in terms of the anharmonic IFCs as [26]:

$$\gamma_\lambda = -\frac{1}{6\omega_\lambda^2}\sum_{\kappa}\sum_{l'\kappa'}\sum_{l''\kappa''}\sum_{\alpha\beta\gamma}\Phi_{\alpha\beta\gamma}(0\kappa,l'\kappa',l''\kappa'')\frac{e_{\alpha\kappa}^{\lambda*}e_{\beta\kappa'}^{\lambda'}}{\sqrt{M_\kappa M_{\kappa'}}}e^{i\mathbf{q}\cdot\mathbf{R}_{l'}}\mathbf{r}_{l''\kappa''\gamma} \quad (8)$$

Here, $\mathbf{R}_l$ is a lattice vector locating the l^{th} unit cell, κ specifies an atom in this cell whose mass is M_κ, and α,β and γ are Cartesian components. The $\Phi_{\alpha\beta\gamma}(0\kappa,l'\kappa',l''\kappa'')$ are third order IFCs, and $e_{\alpha\kappa}^{\lambda}$ is the α^{th} component of the phonon eigenvector for atom κ in mode λ. Finally, $r_{\ell\kappa\gamma}$ is the γ^{th} component of the vector locating the κ^{th} lattice atom in the l^{th} unit cell.

We use the Leibfried and Schlömann expression for k_L to calculate the ratio $k_L(P)/k_L(0)$ at room temperature and with P=125GPa. For this case, we find $V_0(P)/V_0(0)=0.936$, $\omega_D(P)/\omega_D(0)=1.18$ [55] and, using Eq. 8, $\bar{\gamma}(P)/\bar{\gamma}(0)=0.636$ giving $k_L(P)/k_L(0)$=3.97. This is about twice as large as the ratio $k_{pure}(P)/k_{pure}(0)$ calculated from the first principles approach presented in this work. This large difference is not surprising. The Leibfried and Schlömann expression for k_L was derived within a simple Debye model in which the intrinsic scattering was assumed to occur only between acoustic phonons and temperatures were assumed to be above θ_D. Since θ_D ~2000K and, as discussed above, in diamond scattering of acoustic phonons by optic phonons plays an essential role in limiting k_L the Leibfried and Schlömann expression should not be expected to work well for diamond.

As described above, our first-principles approach to phonon thermal transport uses an exact numerical solution of the PBE. This contrasts with other *ab initio* approaches [27, 28, 30-35, 37], which instead use relaxation time approximations (RTAs) to the PBE. In our formulation, this amounts to calculating k_L^0, in place of k_L (see discussion below Eq. 6) and is equivalent to incorrectly treating Normal phonon-phonon scattering processes as resistive. For many materials, this is a good approximation at sufficiently high temperatures where Umklapp

scattering is relatively strong. For example, in Si and Ge, we find less than 10% difference between k_L^0, in place of k_L at T=300K. However, in the carbon based crystals i.e. diamond [26], carbon nanotubes [56], graphene [57] and graphite [58] as well as for boron nitride systems [59, 60] the RTA has been found to work poorly. The stiff bonding and light carbon mass result in a very high frequency scale. The diamond anharmonic scattering rates around room temperature are therefore qualitatively comparable to those of other materials at much lower temperature. Specifically, Normal phonon-phonon scattering plays an important role. This is evident in Fig. 6, which plots the ratio k_L/k_L^0 as a function of temperature for the case of isotopically pure diamond at P=0 and P=125GPa. For both cases the ratio increases with decreasing temperature attaining values of several times k_L^0 in the low temperature region. Note that the ratio is noticeably larger for P=0 compared to P=125GPa. This reflects the decreasing strength of Normal scattering with increasing P, as discussed in connection with Fig. 5.

We briefly comment here on the validity of our use of the LDA for the exchange and correlation functional as compared to the Generalized Gradient Approximation (GGA). At ambient pressure, we have found the calculated phonon dispersion curves and thermal conductivity using the LDA to be in very good agreement with measured values [26]. Furthermore, the calculated LDA phonon frequencies at high symmetry points have been shown to be about as close to measured values as those using the GGA [61]. Figure 14 of Ref. 61 also shows that the linear thermal expansion coefficient calculated using the LDA is in very good agreement with measured data below 500K, the temperature range considered in this work. This validates our use of the LDA for the calculated results presented here. In any case, we emphasize that possible small differences that might exist between LDA and GGA results would not change any of the main findings in this work.

IV. Summary and Conclusions

We have calculated the lattice thermal conductivity, k_L, of diamond as a function of compressive hydrostatic pressure up to several hundred GPa. We find that k_L increases to values well over 10,000$Wm^{-1}K^{-1}$ at room temperature and 400GPa, far higher than any known material. We have identified the primary mechanism for this enhancement as the anharmonic coupling between phonons. The shift of phonon modes to higher frequencies with applied pressure weakens the phonon-phonon scattering rates thereby driving k_L to higher values. The often neglected scattering of heat-carrying acoustic phonons by optic phonons has been shown here to be essential in accurately describing the pressure dependence of k_L. This mechanism is not considered in the frequently used theory of Leibfried and Schlömann [23].

To our knowledge, there are currently no measurements of k_L .vs. P for diamond. While the large values of k_L predicted by the first principles theory presented herein would be challenging to measure for high P, the recent progress in accurate techniques to measure $k_L(P)$ up to tens of GPa [18-21] provides some encouragement. Finally, we note that diamond is unique among all bulk materials in combining extreme bond stiffness with unusually small compressibility and structural phase stability under high compressive pressure. These properties are critical to achieve the record thermal conductivities predicted here.

Acknowledgements

D.A.B. acknowledges support from the National Science Foundation under grant number 1066634. L.L. acknowledges support from DARPA and from the NRC/NRL Research Associateship Program. We also thank Derek Stewart and Natalio Mingo for their useful input.

References

1. http://www.ioffe.ru/SVA/NSM/Semicond/Diamond/index.html
2. L. R. Benedetti, et al., Science 286, 100 (1999).
3. M. Bailes et al., Science 23, 1717 (2011).
4 B. A. Hammel et al., Plasma and Controlled Fusion **4**8, B497 (2006).
5. https://dco.gl.ciw.edu/
6. K. Kunc, I. Loa, and K. Syassen, Phys. Rev. B **68**, 094107 (2003).
7. A. A. Correa, S. A. Bonev and G. Galli, PNAS **103**, 1204 (2006).
8. J. S. Tse and W. B. Holzapfel, J. Appl. Phys. **104**, 043525 (2008).
9. F. Occelli, P. Loubeyer and R. Letoullec, Nature Materials **2**, 151 (2003).
10. M. D. Knudson, M. P. Desjarlais and D. H. Dolan, Science **322**, 1822 (2008).
11. D. K. Bradley, J. H. Eggert, R. F. Smith, S. T. Prisbrey, et al. Phys. Rev. Lett. **102**, 075503 (2009).
12. P.W. Bridgeman, Am. J. Sci. **7**, 81 (1924).
13. D. S. Hughes and F. Sawin, Phys. Rev. **161**, 861 (1967).
14. O. Alm and Bäckström, J. Phys. Chem. Sol. **35**, 421 (1974).
15. .B. Hakansson, P. Andersson and G. Bäckström,, Rev. Sci. Instrum. 59, 2269 (1988).
16. O. Andersson and A. Inaba, Phys. Chem. Chem. Phys. **7**, 1441 (2005).
17. Bin Chen, Wen-Pin Hsieh, David G. Cahill, Dallas R. Trinkle, and Jie Li, Phys. Rev. B **83**, 132301 (2011).
18. Wen-Pin Hsieh, PhD. Thesis, (2011).
19, G. I. Pangilinan, H. D. Ladouceur, and T. P. Russell, Rev. Sci. Inst. **71**, 3846 (2000).

20. Pierre Beck, Alexander F. Goncharov, Viktor V. Struzhkin, Burkhard Militzer, Ho-kwang Mao, and Russell J. Hemley, Appl. Phys. Lett. **91**, 181914 (2007).

21. Wen-Pin Hsieh, Bin Chen, Jie Li, Pawel Keblinski, and David G. Cahill, Phys. Rev B **80**, 180302 (R) (2009).

22. J. M. Ziman, *Electrons and Phonons* (Oxford University Press, London, 1960).

23. G. Leibfried and E. Schlömann, Nach. Akad. Wiss. Gottingen, Math. Phyz. Klasse **4**, 71 (1954).

24. G. A. Slack, in *Solid State Physics* (Academic, New York, 1979) **34**, 1-71.

25. D. A. Broido, M. Malorny, G. Birner, N. Mingo and D. A. Stewart, Appl. Phys. Lett. **91**, 231922 (2007).

26. A. Ward, D. A. Broido, D. A. Stewart and G. Deinzer, Phys. Rev. B **80**, 125203 (2009).

27. Xiaoli Tang, Jianjun Dong, Phys. Earth Planet. Int. **174**, 33 (2009).

28. Nico de Koker, Phys. Rev. Lett. **103**, 125902 (2009).

29. Ward and D. A. Broido, Phys. Rev. B **81**, 085205 (2010).

30. Xiaoli Tang, and Jianjun Dong, Proc. Nat. Acad. Sci. **107**, 4539 (2010).

31. Nico de Koker, Earth and Planet. Sci. Lett. **292**, 392 (2010).

32. Jivtesh Garg, Nicola Bonini, Boris Kozinsky, and Nicola Marzari, Phys. Rev. Lett. **106**, 045901 (2011).

33. Keivan Esfarjani and Gang Chen, Phys. Rev. B **84**, 085204 (2011).

34. Junichiro Shiomi, Keivan Esfarjani, and Gang Chen, Phys. Rev. B **84**, 104302 (2011).

35. A. Kundu, N. Mingo, D. A. Broido, and D. A. Stewart, Phys. Rev. B **84**, 125426 (2011).

36. O. Delaire, J. Ma, K. Marty, A. F. May, M. A. McGuire, M-H. Du, D. J. Somg, A. Podlesnyak, G. Ehlers, M. D. Lumsden and B. Sales, Nature Mat. **10**, 614 (2011).

37. Zhiting Tian, Jivtesh Garg, Keivan Esfarjani, Takuma Shiga, Junichiro Shiomi, and Gang Chen, Phys. Rev. B **85**, 184303 (2012).

38. Wu Li, Natalio Mingo, L. Lindsay, D. A. Broido, D. A. Stewart, and N. A. Katcho, Phys. Rev. B **85**, 195436 (2012).

39. L. Wei, P. K. Kuo, R. L. Thomas, T. R. Anthony and W. F. Banholzer, Phys. Rev. Lett. **70**, 3764 (1993).

40. M. Omini and A. Sparavigna, Phys. Rev. B **53**, 9064 (1996).

41. M. Omini and A. Sparavigna, Nuovo Cimento D **19**, 1537 (1997).

42. J. An, A. Subedi, and D. J. Singh, Solid State Comm. 148, 417 (2008).

43. T. Sun and P. B. Allen, Phys. Rev. B 82, 224305 (2010).

44. S. Baroni *et al.*, http://www.quantum-espresso.org.

45. G. Deinzer, G. Birner, and D. Strauch, Phys. Rev. B **67**, 144304 (2003).

46. G. B. Bachelet, D. R. Hamann and M. Schlüter, Phys. Rev. B **26**, 4199 (1982).

47. H. J. Monkhorst and J. D. Pack, Phys. Rev. B 13, 5188 (1976).

48. S. I. Tamura, Phys. Rev. B **27**, 858 (1983).

49. J. R. Olson, R. O. Pohl, J. W. Vandersande, A. Zoltan, T. R. Anthony and W. F. Banholzer, Phys. Rev. B **47**, 14850 (1993).

50. D. G. Onn, A. Witek, Y. Z. Qiu, T. R. Anthony and W. F. Banholzer, Phys. Rev. Lett. **68**, 2806 (1992).

51. R. Berman, P. R. W. Hudson and M. Martinez, J. Phys. C: Solid State Phys. **8**, L430 (1975).

52. L. Lindsay and D. A. Broido, J. Phys. Cond. Matt. **20**, 165209 (2008).

53. A. Sparavigna, Phys. Rev. B **65**, 064305 (2002).

54. D. A. Broido, A. Ward and N. Mingo, Phys. Rev. B **72**, 014308 (2005).

55. For v_{TA} and v_{LA} we used the calculated acoustic velocities along the [100] direction.

56. L. Lindsay, D. A. Broido and N. Mingo, Phys. Rev. B **80**, 125407 (2009).

57. L. Lindsay, D. A. Broido and N. Mingo, Phys. Rev. B **82**, 115427 (2010).

58. L. Lindsay, D. A. Broido and N. Mingo, Phys. Rev. B **83**, 235428 (2011).

59. L. Lindsay and D. A. Broido, Phys. Rev. B **84**, 155421 (2011).

60. L. Lindsay and D. A. Broido, Phys. Rev. B **85**, 035436 (2012).

61. N. Mounet and N. Marzari, Phys. Rev. B 71, 205214 (2005).

Figure Captions

Figure 1 The calculated P .vs. lattice constant (solid red curve) compared with calculated LDA results from Ref. 6 (black open circles) and the measured data from Ref. 9 (black solid squares).

Figure 2 Density of phonon states in diamond as a function of phonon frequency for P=0 (dashed red curve) and P=125GPa (solid blue curve).

Figure 3 Calculated k_{nat} and k_{pure} as a function of T for P=0 (solid and dashed black curves) and P=125GPa (solid and dashed red curves). Sample size is taken to be L=1mm.

Figure 4 Calculated k_{nat} (solid red curve) and k_{pure} (dashed black curve) .vs. P for diamond at T=300K. Inset shows the calculated maximum phonon energy ω_{LTO} .vs. P (solid black line). Also shown are measured results from Ref. 9 (dashed black line). We note that the calculated ω_{LTO} agrees within 3% of the measured values in Fig. 3 of Ref. 9.

Figure 5 $k_{acc}(l)/\ k_L$ for P=0 and T=300K (solid black curve), P=0 and T=200K (dashed blue curve) and P=125GPa and T=300K (dotted red curve).

Figure 6 Ratio of the room temperature thermal conductivity obtained from the full PBE solution to that from the relaxation time approximation, k_L/k_L^0, for P=0 (dashed black curve), and P=125GPa (solid red curve).

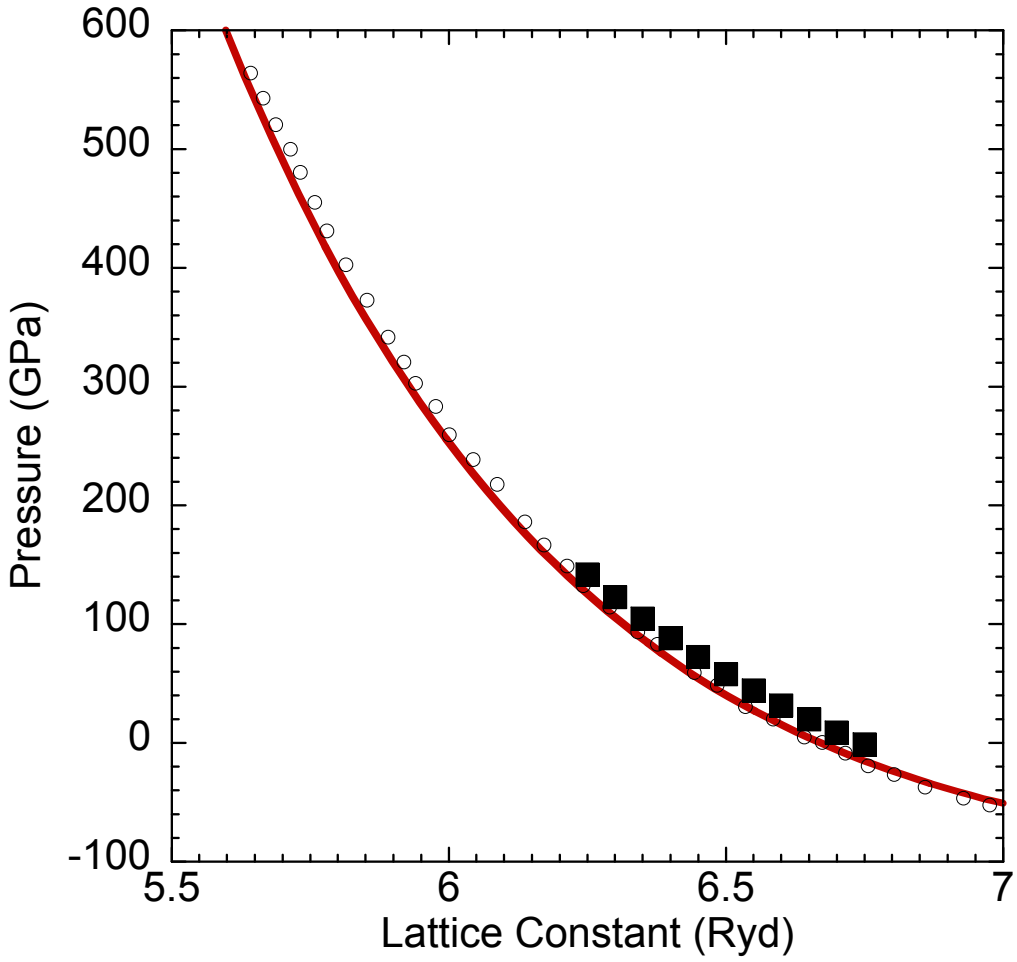
600
500
400
300
200
100
0
-100
Pressure (GPa)
5.5
6
6.5
7
Lattice Constant (Ryd)

Figure 1

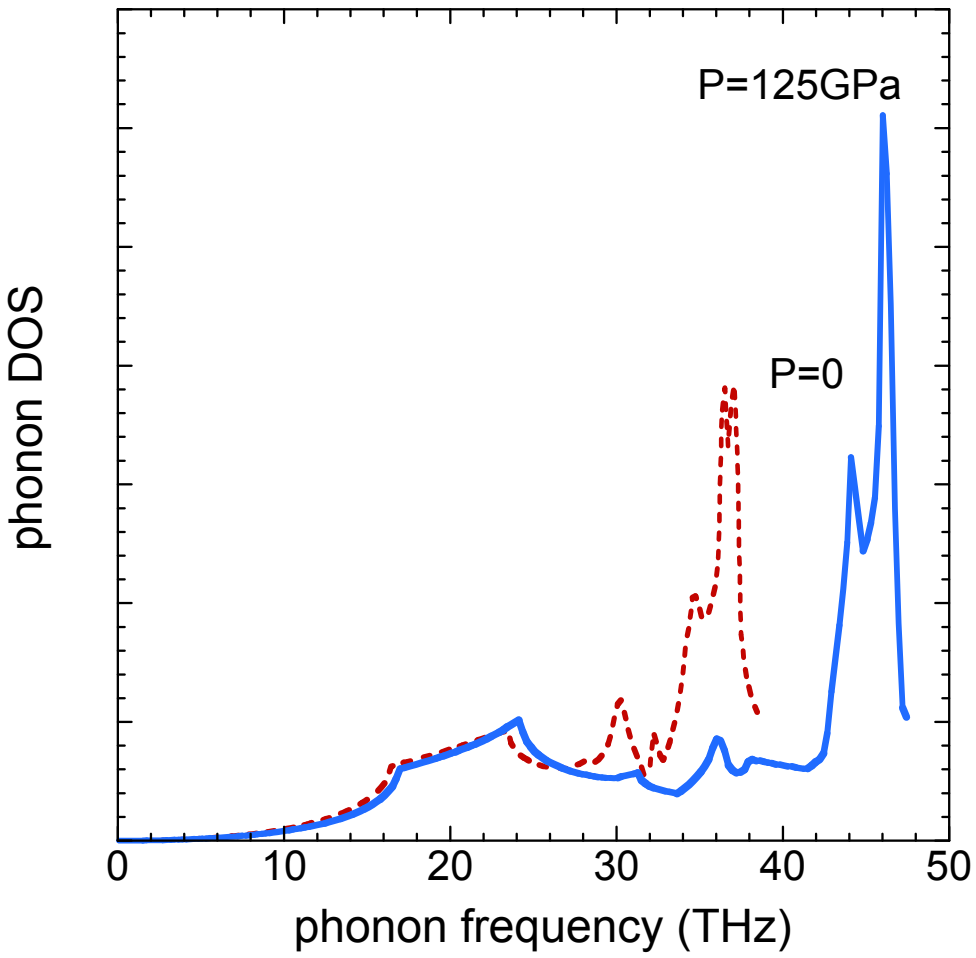

Figure 2

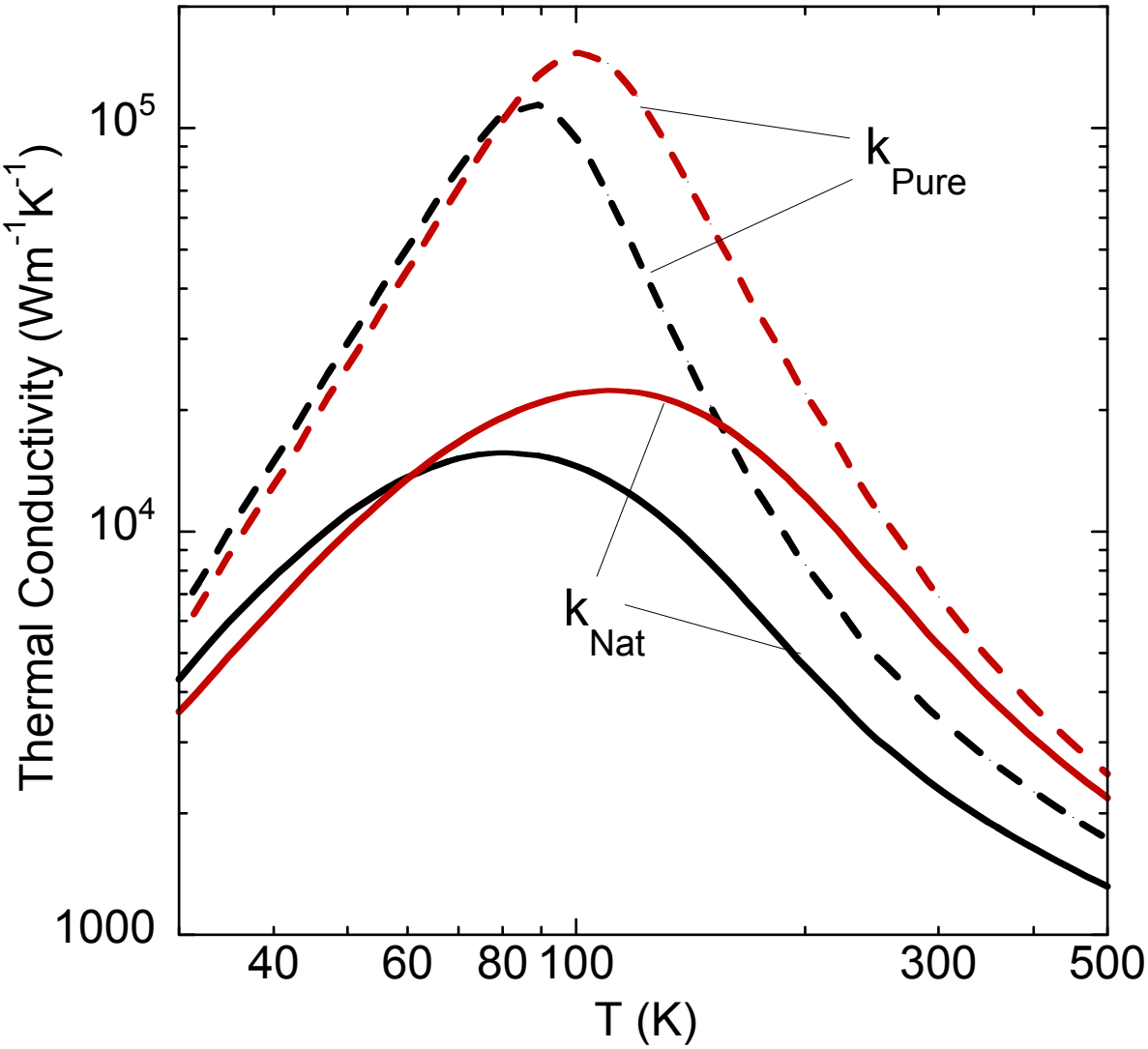
Thermal Conductivity (Wm^{-1}K^{-1})
10^5
10^4
1000
40
60
80
100
300
500
T (K)
k_{Pure}
k_{Nat}

Figure 3

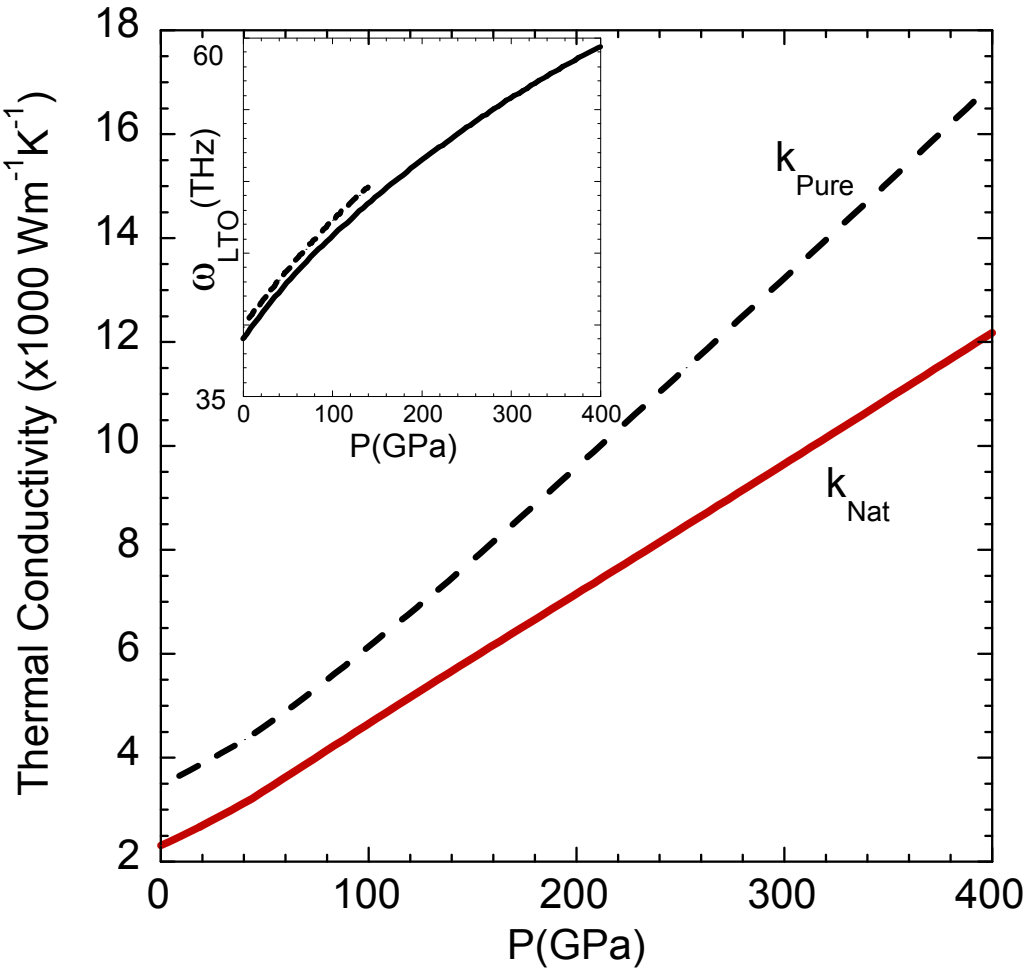
Thermal Conductivity (x1000 Wm-1K-1)
P(GPa)
k Pure
k Nat
ω LTO (THz)
P(GPa)

Figure 4

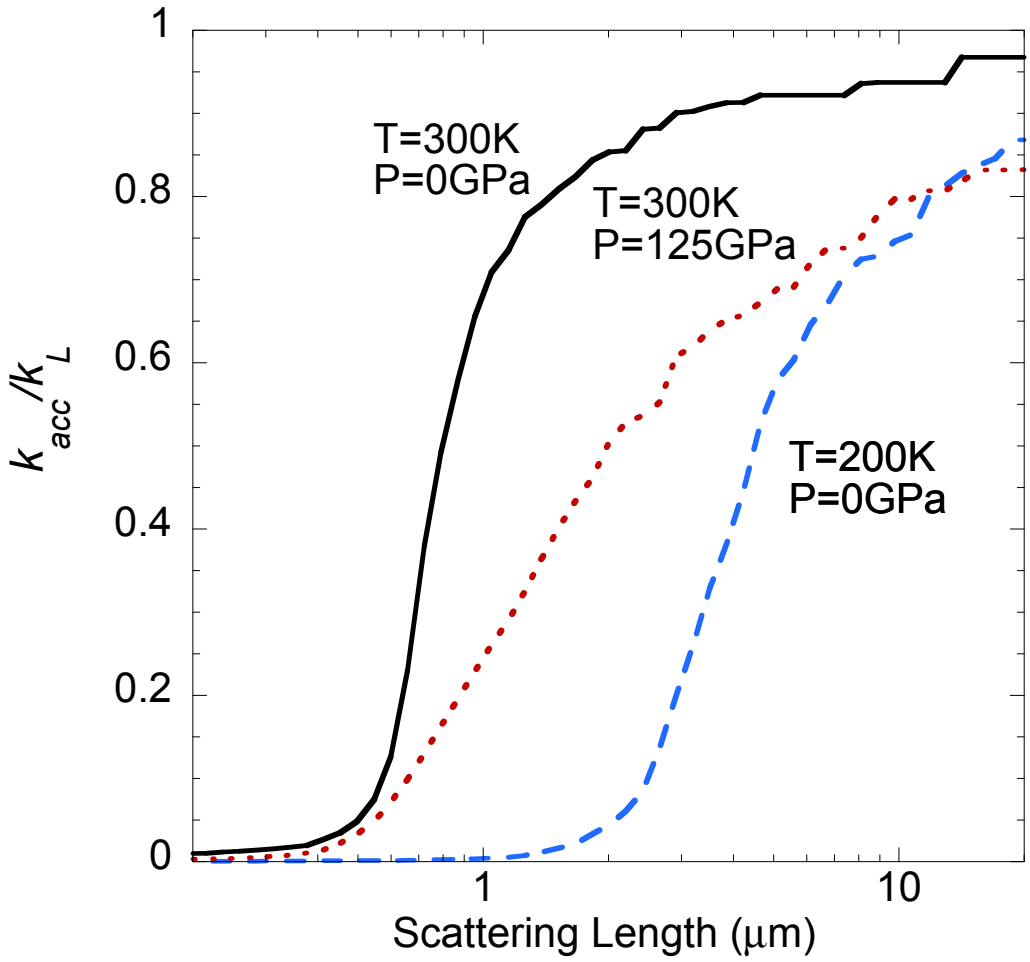
1
0.8
0.6
0.4
0.2
0
k_{acc}/k_L
T=300K
P=0GPa
T=300K
P=125GPa
T=200K
P=0GPa
1
10
Scattering Length (μm)

Figure 5

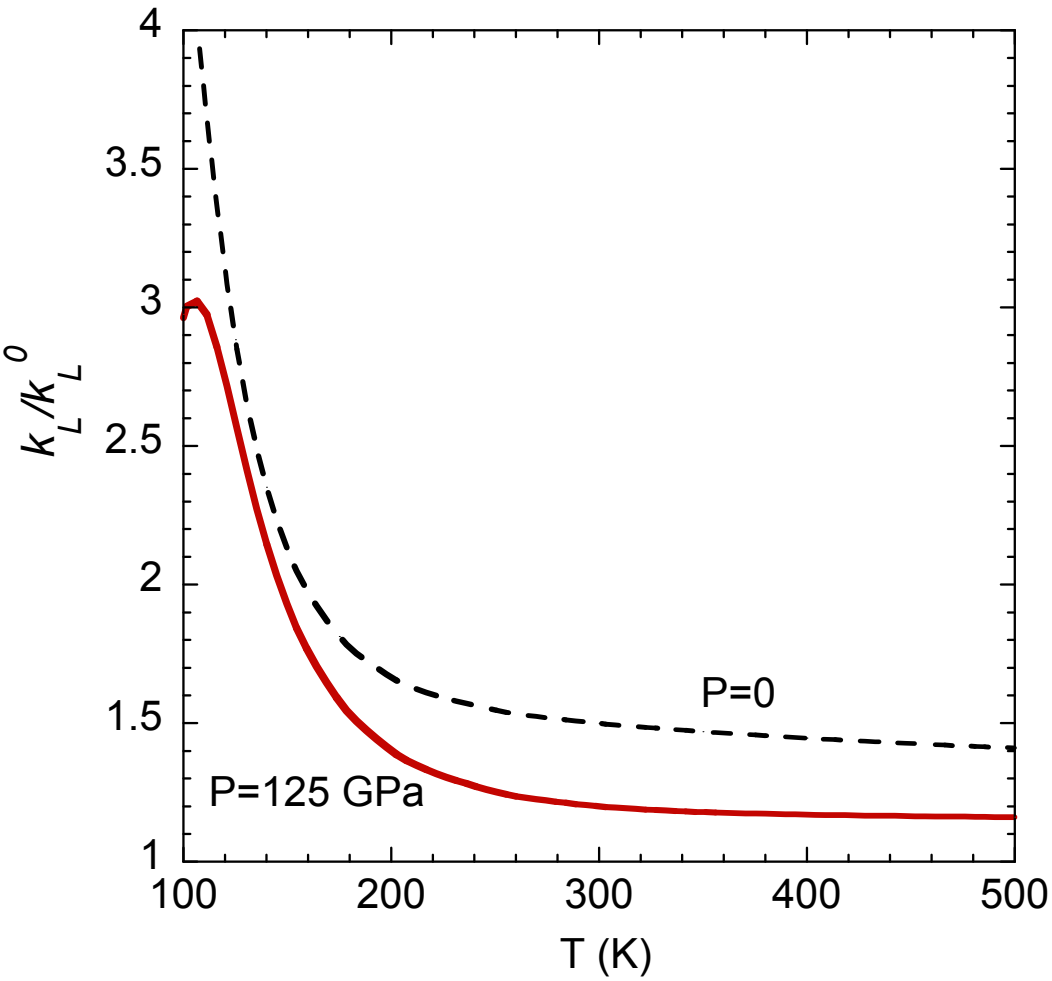

Figure 6